## REPORT

# FAM92A1 is a BAR domain protein required for mitochondrial ultrastructure and function

Liang Wang[1], Ziyi Yan[1] , Helena Vihinen[1] , Ove Eriksson[2] , Weihuan Wang[1,4], Rabah Soliymani[3], Yao Lu[1], Yaxin Xue[1], Eija Jokitalo[1] , Jing Li[4], and Hongxia Zhao[1]

**Mitochondrial function is closely linked to its dynamic membrane ultrastructure. The mitochondrial inner membrane (MIM) can form extensive membrane invaginations known as cristae, which contain the respiratory chain and ATP synthase for oxidative phosphorylation. The molecular mechanisms regulating mitochondrial ultrastructure remain poorly understood. The Bin-Amphiphysin-Rvs (BAR) domain proteins are central regulators of diverse cellular processes related to membrane remodeling and dynamics. Whether BAR domain proteins are involved in sculpting membranes in specific submitochondrial compartments is largely unknown. In this study, we report FAM92A1 as a novel BAR domain protein localizes to the matrix side of the MIM. Loss of FAM92A1 caused a severe disruption to mitochondrial morphology and ultrastructure, impairing organelle bioenergetics. Furthermore, FAM92A1 displayed a membrane-remodeling activity in vitro, inducing a high degree of membrane curvature. Collectively, our findings uncover a role for a BAR domain protein as a critical organizer of the mitochondrial ultrastructure that is indispensable for mitochondrial function.**

## Introduction

Mitochondria possess an intricate membrane architecture defining distinct submitochondrial compartments that are critical for mitochondrial function. In particular, the mitochondrial inner membrane (MIM) is extensively folded into membrane invaginations, which are connected by crista junctions to the inner boundary membrane (IBM; Mannella, 2006). Furthermore, mitochondrial membranes are highly dynamic and undergo constant membrane remodeling by fusion and fission (Wai and Langer, 2016). It has remained enigmatic how the mitochondrial membrane curvature is generated and maintained. Two protein complexes, the mitochondrial contact site and cristae organizing system (MICOS) and the $F_1F_0$-ATP synthase, have been demonstrated to play important roles in defining the cristae membrane (CM) junction and cristae ridges, respectively (Paumard et al., 2002; Strauss et al., 2008; Rabl et al., 2009; Herrmann, 2011; Davies et al., 2012; Friedman and Nunnari, 2014; Pfanner et al., 2014; Barbot et al., 2015; Bohnert et al., 2015; Guarani et al., 2015; Kühlbrandt, 2015; Milenkovic and Larsson, 2015; Cogliati et al., 2016; van der Laan et al., 2016; Hessenberger et al., 2017; Tarasenko et al., 2017). However, the molecular mechanism underlying the biogenesis of MIM invaginations, and in particular whether dedicated membrane-shaping proteins are involved in the processes of curvature generation, remain to be established.

Generation of membrane curvature is an essential process in membrane morphogenesis coordinated by functionally distinct protein families (Prinz and Hinshaw, 2009; Pirozzi et al., 2011). The Bin1-Amphiphysin-Rvs167 (BAR) domain protein family constitutes the largest and most diverse group of membrane-shaping proteins. The BAR domain proteins participate in the dynamic remodeling of the plasma membrane and in intracellular vesicle budding (McMahon and Gallop, 2005; Frost et al., 2009; Qualmann et al., 2011; Zhao et al., 2011; Mim and Unger, 2012; Safari and Suetsugu, 2012; Daumke et al., 2014; McMahon and Boucrot, 2015; Simunovic et al., 2015). However, whether BAR domain proteins are involved in MIM morphogenesis has thus far remained unknown.

## Results and discussion

### FAM92A1 is a mitochondrial protein

BLAST searches identified a novel BAR domain protein FAM92A1, which is highly conserved among mammals (Fig. S1 A). Structure prediction revealed that the BAR domain of FAM92A1 has low sequence identity to the other BAR domains, but the predicted structure displayed a similar fold (Fig. S1, B–D), i.e., the characteristic of BAR domain proteins (Peter et al., 2004). FAM92A1 is

ubiquitously expressed in mouse tissues and different cell lines (Figs. 1 A and S2 A). Interestingly, the endogenous FAM92A1 colocalized with MitoTracker red (Fig. 1 B), suggesting that FAM92A1 resided in mitochondria. Moreover, FAM92A1 was highly enriched in the mitochondrial fraction (Figs. 1 C and S2, B and C). Besides the predominant mitochondrial localization, a small fraction of FAM92A1 appeared to localize in the cytoplasm and nucleus (Fig. S2 D). FAM92A1 did not significantly colocalize with the ER proteins protein disulfide-isomerase (PDI) and calnexin (Fig. S2 E). Only a minor colocalization was found in the perinuclear region that was probably attributable to crowding of mitochondria in this region. To determine the submitochondrial localization of FAM92A1, isolated mitochondria were treated with proteinase K (Fig. 1 D). FAM92A1 was not digested by proteinase K in intact mitochondria and mitoplasts but degraded after solubilization of mitochondria membranes, suggesting that FAM92A1 resided either at the inner surface of MIM or in the matrix. To corroborate these findings, we performed immunoEM of endogenous FAM92A1. The results confirmed that FAM92A1 localized in the mitochondrial matrix in close proximity to the inner membrane and clustered mostly along the cristae (Fig. 1 E). Data quantification revealed that FAM92A1 predominantly localized on the CM (Fig. 1 F). Furthermore, protein extraction with sodium carbonate (Fig. 1 G) revealed that FAM92A1 resided predominantly in the pellet/membrane fraction but was released to the supernatant with increasing pH, indicating that FAM92A1 is a membrane-bound but not integral membrane protein.

FAM92A1 harbors a conserved N-terminal sequence consisting of an alternating pattern of hydrophobic and positively charged amino acids, with only a few negatively charged residues (Fig. S1 A), i.e., the characteristics of a mitochondrial import presequence. To determine the sequence elements required for mitochondrial targeting, we linked the N-terminal 47 aa of FAM92A1 (FAM92A1$_{1-47}$), which ends after a positively charged amino acid cluster, to GFP (Fig. 1 H). Expression of FAM92A1$_{1-47}$-GFP in cells showed an unambiguous mitochondrial localization (Fig. 1 I). To corroborate this finding, we generated an Apex2 construct carrying the 1–47 aa (FAM92A1$_{1-47}$-Apex2; Fig. 1 H). The data confirmed that the N-terminal peptide was sufficient to direct the import of FAM92A1$_{1-47}$ into mitochondria (Fig. 1 J). Furthermore, deletion of 1–47 aa from FAM92A1 (FAM92A1$\Delta_{1-47}$-GFP) resulted in a cytosolic localization (Fig. 1 I), demonstrating that the N-terminal peptide is essential for mitochondrial import of FAM92A1. Immunoblotting showed that the endogenous FAM92A1 migrated at ∼29 kD, whereas the purified his-tagged protein appeared at ∼34 kD (Fig. S2 F), suggesting that the N-terminal sequence was processed after mitochondrial import. Furthermore, FAM92A1$_{1-47}$-GFP displayed two bands with a difference of ∼4 kD (Fig. S2 G), demonstrating that the N-terminal peptide was cleaved off after mitochondrial import. Together, these data reveal that FAM92A1 is a ubiquitously expressed mitochondrial membrane-bound protein localized to the matrix side of the MIM.

## Role of FAM92A1 in mitochondrial function
To gain insight into the function of FAM92A1, we performed loss-of-function experiments using siRNA silencing. Efficient FAM92A1 depletion by siRNA (Figs. 2 A and S2 H) resulted in a

defective cell proliferation in both glucose- and galactose-containing mediums, with a higher inhibition in the presence of galactose, suggesting that the inhibition of cell growth was mainly due to mitochondrial defects (Fig. 2 B). Furthermore, down-regulation of FAM92A1 significantly diminished the mitochondrial membrane potential (Fig. 2 C) and increased the oxidative stress in mitochondria and cytoplasm (Fig. 2, D and E; and Fig. S2 I), indicating that FAM92A1 knockdown results in mitochondrial functional defects. Indeed, FAM92A1-knockdown cells displayed a profound decrease in the cellular oxygen consumption rate (OCR) and respiratory capacities compared with control cells (Fig. 2, F and G). In agreement with these data, the cellular ATP production was significantly decreased (Fig. 2 H). Importantly, the defects in mitochondrial membrane potential, cellular ATP production, OCR, and elevated oxidative stress caused by FAM92A1 knockdown can be rescued by WT FAM92A1 (Fig. 2, C–H), suggesting that these changes were specific effects of FAM92A1 silencing. Furthermore, down-regulation of FAM92A1 induced a perturbation in the complex assembly and enzyme activities of complexes I and IV of the electron transport chain (Fig. 2, I and J), while the steady-state level of respiratory chain components and DNA copy number remained unaffected (Figs. 2 K and S2 J). Moreover, the changes in the complexes I and IV can be rescued by WT FAM92A1 (Fig. 2, J and I). Collectively, these data demonstrated that FAM92A1 is important for mitochondrial function.

## Regulation of mitochondrial morphology and inner membrane ultrastructure by FAM92A1
Mitochondrial function is closely linked to organelle morphology and structure. Therefore, we examined the mitochondrial morphology following down-regulation of FAM92A1. The results revealed that depletion of FAM92A1 induced dramatic changes of mitochondrial morphology with the appearance of abnormal spherical and fragmented mitochondria, in contrast with the tubular mitochondrial network in control cells (Fig. 3, A and B). In addition, the mitochondrial dynamics was drastically impaired in FAM92A1-knockdown cells (Videos 1 and 2), and the resulting bleb-shaped mitochondria remained separated and exhibited pronounced fission and fusion defects.

To assess the mitochondrial ultrastructural changes after depletion of FAM92A1 and determine whether FAM92A1 is required for mitochondrial ultrastructural organization, cells treated with FAM92A1 siRNA were analyzed by transmission EM. Strikingly, FAM92A1 knockdown caused drastic changes in MIM architecture (Fig. 3, C and D; and Videos 3, 4, and 5). A majority of mitochondria in FAM92A1-knockdown cells had a reduced quantity of membrane invagination along with membrane remodeling instead of elongated narrow invaginations present in control cells. Frequently, the mitochondria in FAM92A1-knockdown cells were devoid of membrane invaginations. Quantification of the membrane structure profile revealed that not only the mitochondrial diameter increased (Fig. 3 E) but also that the percentage of mitochondria with lamellar cristae and number of lamellar cristae per mitochondrial length decreased significantly (Fig. 3, F and G). Furthermore, the length of cristae clearly decreased (Fig. 3 H). In contrast, FAM92A1 silencing did not change the opening of
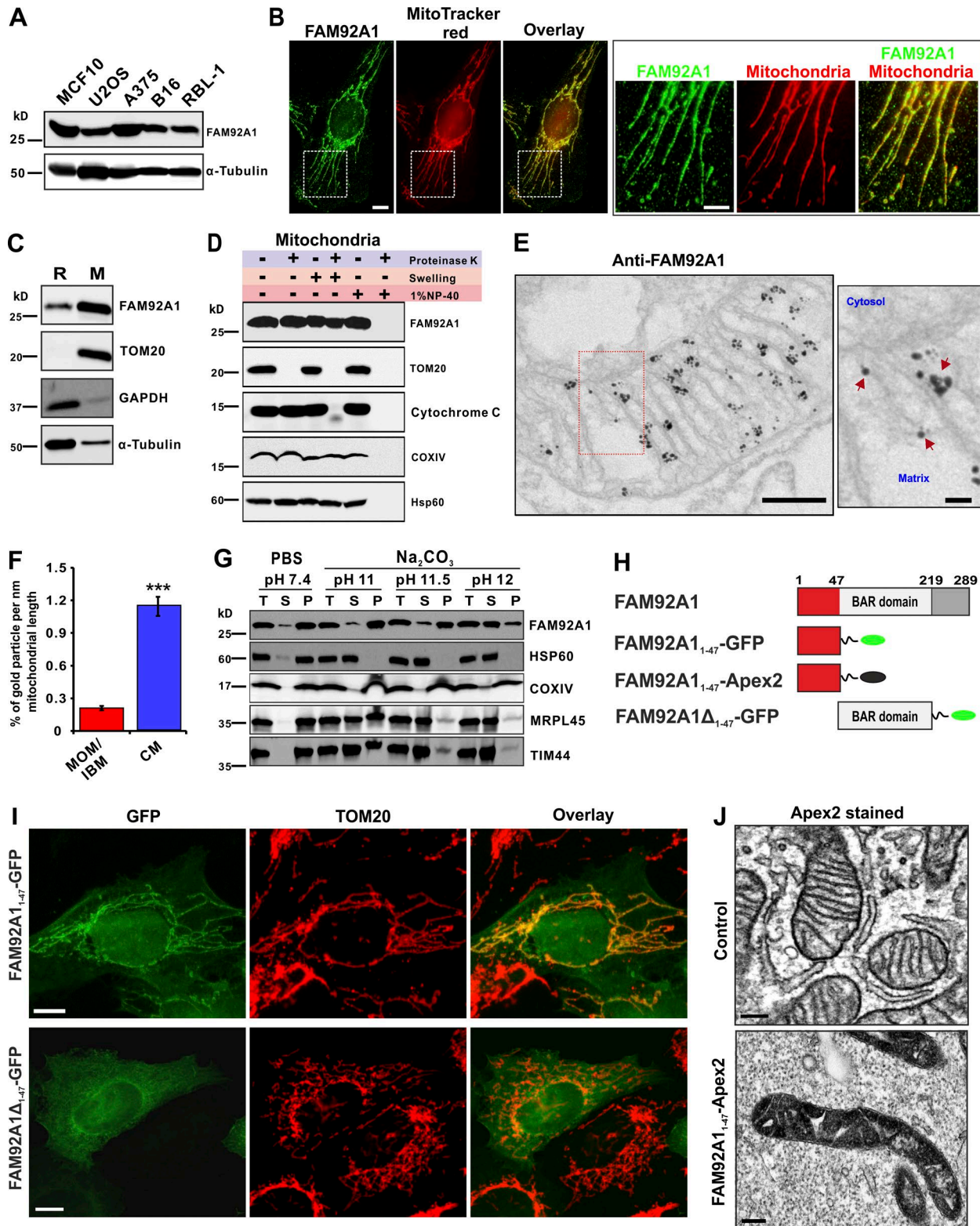
Wang et al.
Regulation of mitochondrial ultrastructure by FAM92A1

**Journal of Cell Biology** 98
https://doi.org/10.1083/jcb.201806191

Figure 1. **FAM92A1 is a ubiquitously expressed mitochondrial protein. (A)** Western blot analysis of FAM92A1 expression in different cell lines. **(B)** Immunofluorescence staining of U2OS cells for endogenous FAM92A1. Bars: 10 μm (main images); 5 μm (insets). **(C)** Western blot analysis to examine the subcellular localization of FAM92A1. M, mitochondrial fraction (pellet [P]); R, rest fraction except mitochondria (the supernatant [S]) after final centrifugation at 7,000 $g$. **(D)** Protease digestion of isolated mitochondria with proteinase K. TOM20, cytochrome c, COXIV, and Hsp60 were used as mitochondrial protein controls in different submitochondrial compartments. **(E)** ImmunoEM of endogenous FAM92A1. Bars: 200 nm (main images); 50 nm (inset). The red arrows indicate FAM92A1. **(F)** Quantification of immunogold particle distribution in the MOM/IBM and CM. ***, P ≤ 0.001, Student's $t$ test. **(G)** Mitochondrial protein extraction by sodium carbonate. T, total mitochondria. **(H)** Schematic diagram of FAM92A1 N-terminal peptides with different tags. **(I)** Immunofluorescence images of cells transfected with FAM92A1$_{1-47}$-GFP and FAM92A1$_{\Delta1-47}$-GFP for 24 h. Bars, 10 μm. **(J)** Transmission EM analysis of mitochondrial import of FAM92A1$_{1-47}$-Apex2. Bars, 200 nm.
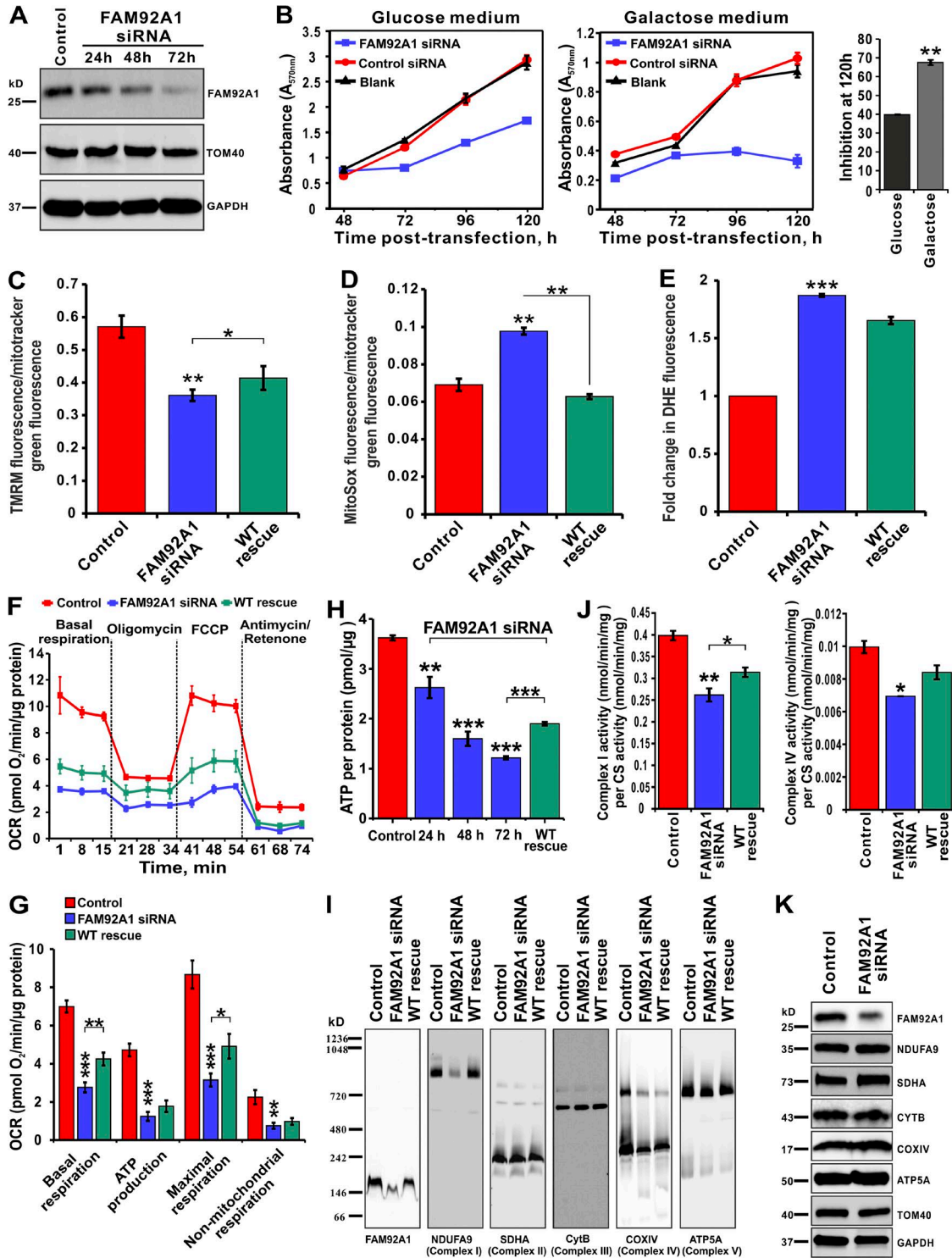
Figure 2. **Down-regulation of FAM92A1 caused defects in mitochondrial function. (A)** FAM92A1 siRNA induced efficient silencing of FAM92A1. **(B)** Cell proliferation in glucose or galactose medium after depletion of FAM92A1 was determined using MTT assays. The cell growth inhibition at 120 h is shown in the bar graph. **(C)** Mitochondrial membrane potential was detected with TMRM staining. **(D)** Superoxide species in mitochondria were detected by MitoSOX. **(E)** Production of cellular ROS was detected by dihydroethidium. **(F)** OCR was measured using a Seahorse XF96ᵉ Analyzer. **(G)** Statistical analysis of OCR in F. **(H)** Changes of the cellular ATP levels after FAN92A1 knockdown and rescue by WT FAM92A1. **(I)** Effects of FAM92A1 down-regulation on complex assembly of complexes I–V and rescue by WT FAM92A1. **(J)** Effects of FAM92A1 knockdown on the enzyme activities of complex I and IV and rescue by WT FAM92A1. The enzyme activity was normalized to the protein amount and the corresponding activity of citrate synthase (CS). **(K)** The steady-state level of respiratory chain components in FAM92A1-knockdown cells. In C–J, WT FAM92A1 was expressed in cells after 20 h siRNA treatment. Cells were harvested after 48 h expression of WT FAM92A1. Error bars indicate ± SEM. *, $P \leq 0.05$; **, $P \leq 0.01$; ***, $P \leq 0.001$, Student's $t$ test.

Wang et al.
Regulation of mitochondrial ultrastructure by FAM92A1

**Journal of Cell Biology**          100
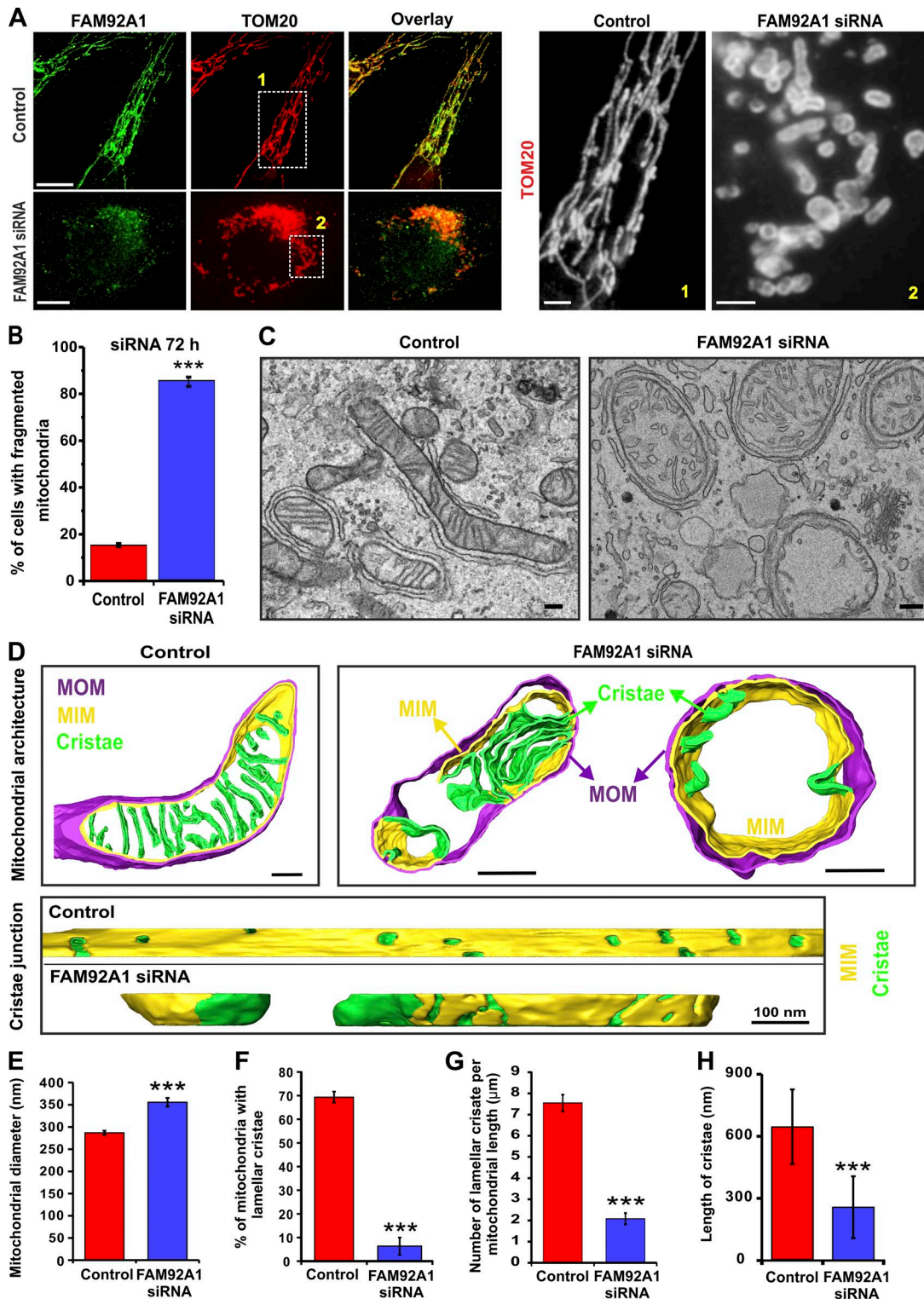https://doi.org/10.1083/jcb.201806191

Figure 3.   **FAM92A1 depletion resulted in abnormal mitochondrial morphology and inner membrane ultrastructure (A) Immunofluorescence images of mitochondrial morphology after treatment with siRNA for 72 h.** Bars: 10 µm (main images); 2 µm (insets). **(B)** Quantification of cells with fragmented mitochondria after FAM92A1 was depleted for 72 h. At least 250 cells each from the control and FAM92A1-knockdown cells were analyzed. **(C)** Transmission EM images of mitochondria in U2OS cells treated with siRNA for 72 h. Bars, 200 nm. **(D)** ET of mitochondria in control and FAM92A1-knockdown cells. The outer membrane (purple), inner membrane (yellow), and cristae (green) were superimposed on a tomographic slice and viewed from the top and side. Bars, 200 nm. **(E–H)** Quantification of the MIM ultrastructural profile including mitochondrial diameter (E), percentage of mitochondria with lamellar cristae (F), number of lamellar cristae per mitochondrial length (G), and length of cristae (H). At least 200 mitochondria were used for mitochondrial morphology analysis (E and F). At least 100 mitochondria was used for analyzing the number of lamellar cristae per mitochondrial length (G). 214 and 236 cristae were used for analyzing the cristae length in control and FAM92A1 siRNA–treated cells, respectively (H). Error bars indicate mean ± SEM. ***, $P \leq 0.001$, Student's $t$ test.

crista junctions significantly (Fig. S2 K), but the number of crista junctions decreased (Fig. S2 K and Videos 6 and 7). Moreover, the assembly of the MICOS complex decreased following FAM92A1 knockdown (Fig. S2 L). Loss of membrane invagination due to FAM92A1 knockdown may affect the stability of MICOS complex and cause protein degradation. However, in the already-formed membrane invaginations, MICOS retained to maintain the normal cristae junction openings. Taken together, these data indicate that FAM92A1 is essential for maintaining mitochondrial morphology and inner membrane ultrastructure.

### Interaction of FAM92A1 with mitochondrial membranes

To examine whether FAM92A1 binds directly to the MIM, we produced recombinant full-length FAM92A1 and its BAR domain (1–219 aa; Figs. 4 A and S2 M). The purified FAM92A1 BAR domain exists mainly as dimers in equilibrium with a minor quantity as oligomers (Fig. 4 B), displaying the canonical character of the BAR domains (Habermann, 2004; Mim et al., 2012). Vesicle cosedimentation assays using membranes having a lipid composition characteristic of the mitochondrial outer membrane (MOM) and MIM (Watt et al., 2002; Horvath and Daum, 2013) showed that the full-length FAM92A1 bound to the mitochondrial model membranes with a similar affinity for MOM and MIM (Figs. 4 C and S2 N). The BAR domain binds to membranes with a lower affinity compared with the full-length FAM92A1. Our results indicated that the N-terminal peptide of FAM92A1 was cleaved off after mitochondrial import (Fig. S2, F and G), and mitofate analysis indicated that the N-terminal peptide is cleaved at position K40 (Fig. 4 A). Therefore, we also examined the membrane interaction of FAM92A1 lacking the 1–40 aa (FAM92A1$\Delta_{1-40aa}$). The results revealed that FAM92A1$\Delta_{1-40aa}$ remained bound to the membranes but with a lower affinity compared with the full-length protein (Fig. 4, C and D). Investigating further the lipid-binding specificity of FAM92A1, we found that it bound to the phosphatidylcholine (PC):phosphatidylethanolamine (PE) membrane but that the membrane association was significantly augmented in the presence of PI(4,5)$P_2$ or cardiolipin (Figs. 4 D and S2 O), suggesting that FAM92A1 preferentially binds to the negatively charged phospholipids. This finding is in line with the characteristic preference for negatively charged phospholipids shared by all BAR domain proteins (McMahon and Boucrot, 2015).

Interestingly, the membrane association of FAM92A1 increased the 1,6-diphenyl-1,3,5-hexatriene (DPH) anisotropy (Fig. 4 E), which reports the changes in rotational intramembrane motion induced by protein insertion into the lipid bilayer (Zhao et al., 2013), suggesting that FAM92A1 inserted into the hydrophobic region of lipid bilayer. FAM92A1 displayed more pronounced effects on DPH anisotropy in the MIM, while in the absence of cardiolipin, membrane insertion decreased significantly, indicating that cardiolipin enhanced the membrane insertion. Interestingly, FAM92A1$\Delta_{1-40aa}$ displayed much less effect on DPH anisotropy, providing evidence that the N-terminal peptide facilitates membrane insertion before cleavage. Together, these data demonstrate that FAM92A1 directly interacts with membranes having a lipid composition characteristic of the MIM and that FAM92A1 preferentially interacts with the negatively charged phospholipids.

### Membrane remodeling by FAM92A1

Having demonstrated that FAM92A1 binds to mitochondrial model membranes, we asked whether FAM92A1, like other BAR domain proteins, can directly sculpt the membrane structure. Strikingly, the full-length FAM92A1 and its BAR domain transformed spherical liposomes into narrow tubules (Fig. 4, F and G), suggesting that FAM92A1 possesses membrane-remodeling activity. The diameter of membrane tubules is similar to that of the tubules induced by classical BAR domain proteins (Gallop et al., 2006), with an average of 32 nm (Fig. 4 H). Importantly, FAM92A1$\Delta_{1-40aa}$ retained the membrane-remodeling activity and generated membrane tubules with a diameter of 19.97 nm (Figs. 4, F–H), significantly narrower than the tubules induced by the full-length protein (Fig. 4 H). This is due to membrane insertion of the N terminus of the full-length FAM92A1, which can change the spontaneous membrane curvature and regulate the diameter of membrane tubules (Gallop et al., 2006; Campelo et al., 2008; Saarikangas et al., 2009; Boucrot et al., 2012). Interestingly, FAM92A1 caused significant membrane tubulation in the absence of PI(4,5)$P_2$ in the MIM (Fig. S2 P), suggesting that PI(4,5)$P_2$ is not essential for membrane tubulation of the MIM. Furthermore, the full-length FAM92A1, the BAR domain, and FAM92A1$\Delta_{1-40aa}$ induced significant membrane protrusions of giant vesicles when added from the outside (Fig. 4, I and J), demonstrating that FAM92A1 can generate positive membrane curvatures similar to the other BAR domain proteins (Qualmann et al., 2011; McMahon and Boucrot, 2015). Taken together, our data reveal that FAM92A1 displays membrane-remodeling activity by inducing a high degree of positive membrane curvature, indicating the key function of FAM92A1 in regulating mitochondrial membrane ultrastructure.

### Rescue of mitochondrial morphology and inner membrane architecture by FAM92A1

Because FAM92A1 preferentially interacted with the negatively charged phospholipids, we mutated seven clusters of arginines and lysines to alanines (Fig. 5 A). The results revealed that three mutants (Mut3, Mut5, and Mut 7) had impaired lipid-binding activity (Fig. 5, A and B; and Fig. S3 A), suggesting that these three positively charged amino acid clusters formed the membrane-binding interface, with two binding sites residing in the BAR domain module and one at the C-terminal region. Furthermore, the mutants with defects in membrane binding (Mut3, Mut5, Mut7, and Mut5+7) displayed significantly less membrane remodeling activity although the mutants retained some membrane tubulation capability (Fig. 5, C–E).

Subsequently, to verify whether the changes of mitochondria morphology and membrane architecture in FAM92A1-depleted cells were specific effects of FAM92A1 silencing, we performed rescue experiments. The WT FAM92A1 or mutants with/without a tag (Fig. S3 B) was reexpressed in FAM92A1-knockdown cells for the rescue experiments because the FAM92A1 siRNA targeted to the 3′ UTR region. As shown in the representative images in Fig. S3 C and the quantification data in Fig. S3 D, the percentage of fragmented mitochondria in WT FAM92A1-expressed cells were significantly decreased compared with that in FAM92A1-depleted cells. The rescue efficiencies with untagged
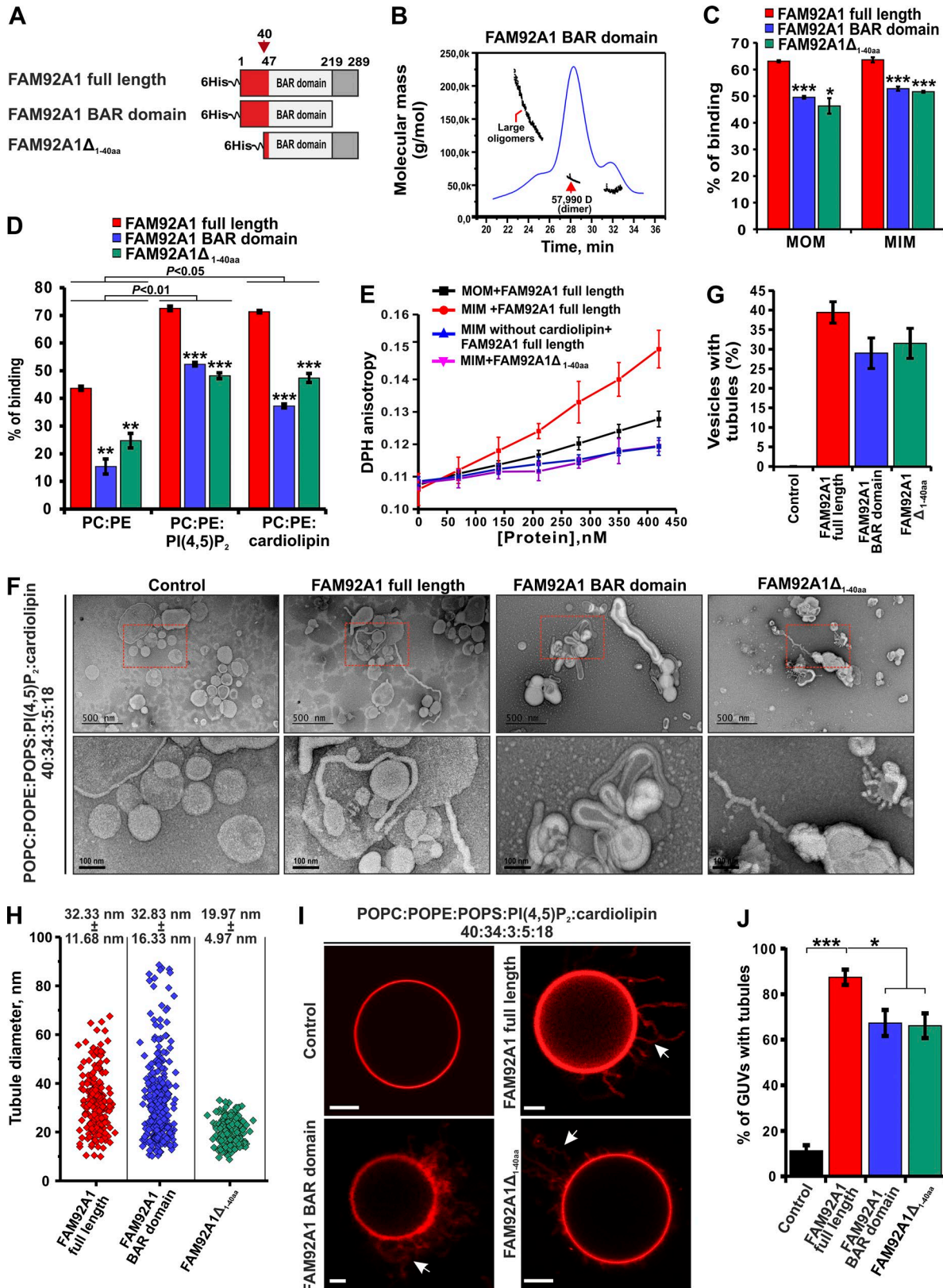
Wang et al.
Regulation of mitochondrial ultrastructure by FAM92A1

**Journal of Cell Biology** 102
https://doi.org/10.1083/jcb.201806191

Figure 4. **FAM92A1 binds the mitochondrial membrane and induces a high degree of positive membrane curvature. (A)** Schematic diagram of his-tagged full-length FAM92A1, its BAR domain, and FAM92A1$\Delta_{1-40aa}$. The putative cleavage site is indicated with a red arrow. **(B)** The BAR domain of FAM92A1 mainly forms dimers in solution, in equilibrium with minor higher-molecular-weight oligomers as determined by multiangle light scattering. **(C)** Vesicle cosedimentation assay for the interaction of FAM92A1 with mitochondrial model membranes. **(D)** Vesicle cosedimentation assay for lipid-binding specificity of FAM92A1. PI(4,5)P$_2$ was included as the same amount as in vivo cardiolipin quantity in the MIM. **(E)** Changes in DPH anisotropy upon membrane association of the full-length FAM92A1 and FAM92A1$\Delta_{1-40aa}$. **(F)** Membrane tubulation of unilamellar vesicles with a lipid composition of the MIM by full-length FAM92A1, its BAR

and GFP- and myc-tagged WT FAM92A1 were not significantly different (Fig. S3 D). Furthermore, we performed the rescue experiments using untagged WT FAM92A1 or mutants (Fig. S3, E and F). Importantly, the changes caused by FAM92A1 knockdown in the ATP level, OCR, and the assemblies of complexes I and IV can be rescued by WT FAM92A1, while the mutants with defects in membrane binding/remodeling displayed less rescue capability (Fig. 5, F and G; and Fig. S3, G and H). Strikingly, expression of WT FAM92A1 significantly reduced the fraction of severely impaired mitochondria and increased the fraction of mitochondria with WT-like cristae structure (Fig. 5, H–J). In addition, WT FAM92A1 clearly rescued the severe structural defects of MIM found in FAM92A1-depleted cells (Fig. 5, H–L). However, the BAR domain and mutants with defects in membrane binding and remodeling only partially rescued the mitochondrial morphology and inner membrane ultrastructure, with obviously reduced rescue capability compared with WT FAM92A1 (Fig. 5, H–L; and Fig. S3 C). Taken together, these data demonstrated that the abnormal MIM ultrastructure and function caused by depletion of FAM92A1 can be specifically rescued through reexpressing FAM92A1, providing strong evidence that FAM92A1 plays an essential role in MIM curvature generation and mitochondrial function.

## Materials and methods

### Materials
1-Palmitoyl-2-oleoyl-*sn*-glycero-3-PC (POPC), 1-palmitoyl-2-oleoyl-*sn*-glycero-3-PE (POPE), 1-palmitoyl-2-oleoyl-*sn*-glycero-3-phosphatidylserine (POPS), cardiolipin, and brain PI(4,5)$P_2$ were purchased from Avanti Polar Lipids. Rhodamine DHPE (L-1392) and DPH were from Thermo Fisher Scientific. MitoTracker green FM and Red CMXRos were from Thermo Fisher Scientific.

### Plasmid construction
FAM92A1 was cloned into pEGFP-N1 plasmid between the XhoI and BamHI and pHAT between SpeI and NsiI cloning sites. GFP was replaced with Apex2 for the Apex2 construct between BamH1 and NotI. Inserts were sequenced to confirm the cloning.

### Cell culture and transient transfection
Human osteosarcoma (U2OS) cells were cultured in DMEM containing 10% FBS (Gibco) and penicillin-streptomycin (Gibco) in a humidified 95% air/5% $CO_2$ incubator at 37°C. For transient transfections, U2OS cells were plated onto six-well tissue culture plates at a density of $2 \times 10^5$ cells per well, and cells were transfected the next day with DNA constructs using FugeneHD reagent (Roche). Cells were subsequently fixed with 4% PFA or replated on fibronectin-coated (10 mg/ml fibronectin) glass-bottomed dishes (MatTek) for live-cell imaging. For the rescue experiments, the rescue constructs were transfected after 20 h control or FAM92A1 siRNA treatment and expressed for 24 or 48 h. The

total time for FAM92A1 silencing was 44 or 68 h. It is important to note that the transfection efficiency of the rescue constructs was decreased by FAM92A1 knockdown (~30–40%). FAM92A1 siRNA targets to the 3′ UTR region and thus WT FAM92A1, and mutants with defects in membrane deformation in vitro were used for the rescue experiments in vivo.

For siRNA silencing, FAM92A1 siRNA (Hs_LOC137392_2; the siRNA sequence was 5′-AAGCCTCAAAGTGAAGTCCAA-3′; QIAGEN) were transfected into cells using Lipofectamine RNAi-MAX (Thermo Fisher Scientific) according to the manufacturer's instructions. U2OS cells were seeded onto a six-well plate at a density of $2 \times 10^5$ cells per well, and for each well, 30 pmol FAM92A1 siRNA or negative control siRNA (SI03650318; QIAGEN) was transfected. The transfected cells were incubated at indicated time points for efficient depletion of the target protein.

### Assays for cell proliferation
Cell proliferation was determined using thiazolyl blue tetrazolium bromide reagent (MTT; M2128; Sigma-Aldrich). Briefly, U2OS cells were cultured with DMEM containing 4.5 g/liter glucose or 0.9 g/liter galactose. MTT solution was added 48, 72, 96, and 120 h after siRNA treatment at a final concentration of 0.5 mg/ml. The medium was subsequently discarded after the incubation with MTT at 37°C for 4 h. Subsequently, 150 µl DMSO was added to dissolve the formazan, and the quantity of formazan was measured by the absorbance at 570 nm using a Varioskan LUX multimode microplate reader with SkanIt Software 5.0 (Thermo Fisher Scientific).

### Immunofluorescence microscope
U2OS cells were grown on coverslips and fixed with 4% PFA for 20 min, washed three times with PBS, and permeabilized for 5 min with 0.1% Triton X-100 in PBS. For antibody staining, permeabilized cells were blocked with Dulbecco plus 0.2% BSA for 30 min and incubated with primary antibody for 1 h at 37°C. Coverslips were washed with Dulbecco plus 0.2% BSA and incubated with fluorescence-conjugated secondary antibody for 1 h at RT. For MitoTracker staining, live cells were incubated with 100 nM MitoTracker red (M7512; Thermo Fisher Scientific) for 15 min and washed three times with medium before fixation. Cells were mounted in Mowiol supplemented with DABCO and imaged with DM6000B microscope (Leica Biosystems) equipped with a Hamamatsu Orca-Flash 4.0 V2 sCMOS camera and LAS-X software (Leica Microsystems) using 63× 1.4-0.60 HCX Plan Apochromat objective and the Semrock BrightLine filters GFP-4050B (excitation, 466/40 nm; emission, 525/50 nm) and TRITC-B (excitation, 543/22 nm; emission, 593/40 nm).

### Live-cell imaging
U2OS cells were treated with FAM92A1 siRNA for 72 h, and the cells were replated on 10 µg/ml fibronectin-coated glass-

domain, and FAM92A1Δ$_{1–40aa}$. **(G)** Quantification of vesicles with tubules in F. At least 300 vesicles were used for quantification. **(H)** Column scatter graph for quantifying the tubule diameter in F. At least 200 membrane tubules were used for analysis. **(I)** The untagged full-length FAM92A1, its BAR domain, and FAM92A1Δ$_{1–40aa}$ induced membrane tubulation in giant unilamellar vesicles (GUVs) with a lipid composition of the MIM. The arrows indicate membrane tubules. **(J)** Quantification of giant vesicles with tubules in I. Bars, 2.5 µm. *, P ≤ 0.05; **, P ≤ 0.001; ***, P ≤ 0.001, Student's *t* test.

Wang et al.
Regulation of mitochondrial ultrastructure by FAM92A1

Journal of Cell Biology    104
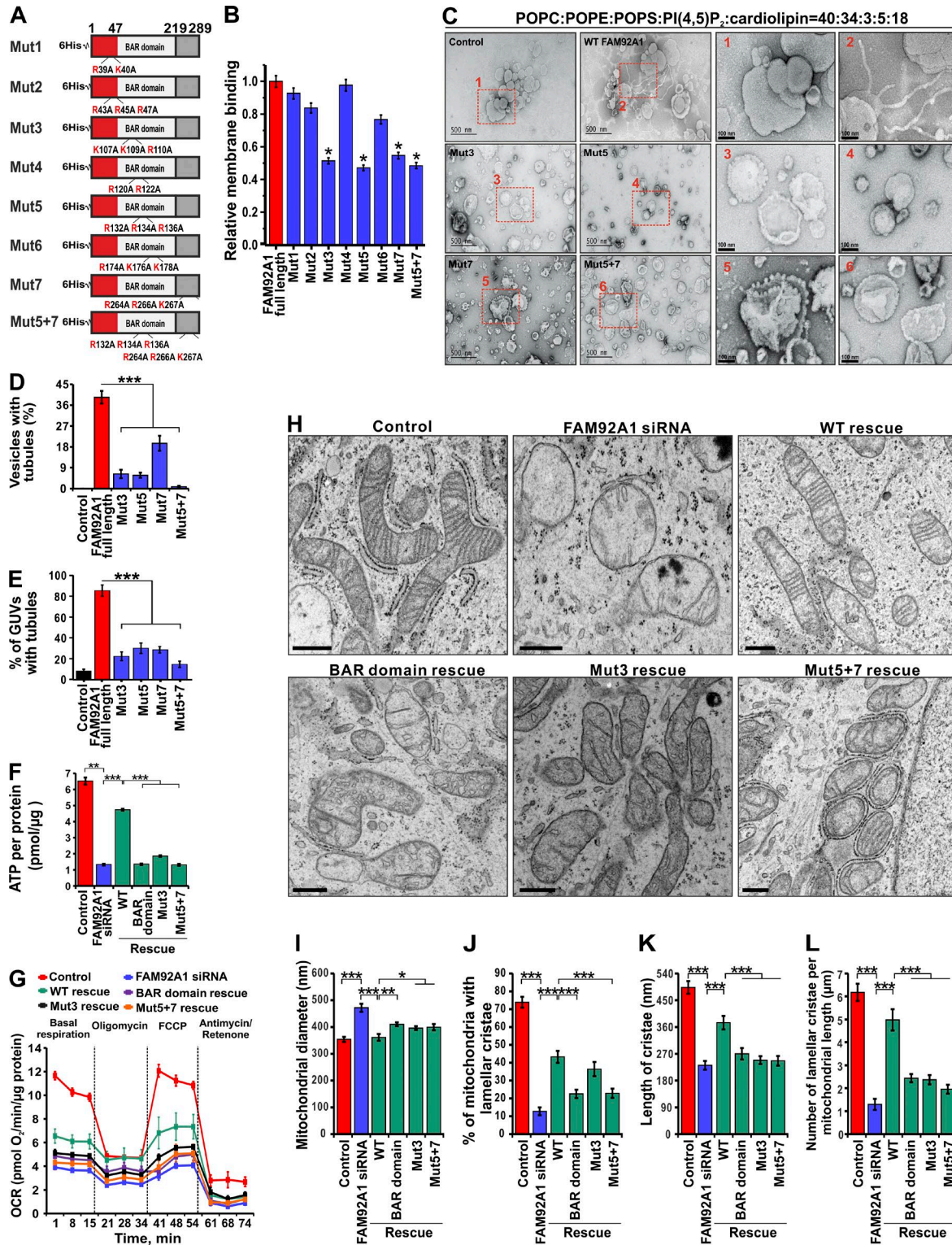https://doi.org/10.1083/jcb.201806191

Figure 5. **Rescue of mitochondrial morphology and ultrastructure by FAM92A1 and mutants. (A)** Schematic diagram of mutated sites in different FAM92A1 mutants. **(B)** A vesicle coflotation assay was used to map the membrane-binding sites of FAM92A1. **(C)** EM showed the membrane tubulation of unilamellar vesicles by WT FAM92A1 and the mutants. **(D)** Quantification of membrane tubulation in C. At least 600 vesicles were used for quantification. **(E)** Quantification of membrane tubulation in giant unilamellar vesicles (GUVs) by WT FAM92A1 and mutants. **(F)** Rescue of the cellular ATP levels by WT FAM92A1 and mutants. **(G)** Rescue of OCR changes caused by FAM92A1 knockdown by expressing WT FAM92A1 or mutants. **(H)** Representative transmission EM image of mitochondria after expressing WT FAM92A1 and mutants in FAM92A1-depleted cells. Bars, 500 nm. **(I–L)** Quantification in mitochondrial diameter (I), percentage of mitochondria with lamellar cristae (J), length of cristae (K), and number of lamellar cristae per mitochondrial length (L). At least 200 mitochondria (F), 300 mitochondria (G), 200 cristae (H), and 100 mitochondria (I) were used for analysis. Error bars indicate mean ± SEM. *, P ≤ 0.05; **, P ≤ 0.01; ***, P ≤ 0.001, Student's *t* test. In F–L, WT FAM92A1 and mutants were transiently expressed for 24 h in FAM92A1-depleted cells after treatment with FAM92A1 siRNA for 20 h. The total time for control or FAM92A1 siRNA treatment was 44 h.

bottomed dishes (MatTek) after 48 h transfection of mitochondrial matrix–targeted YFP (mito-YFP). The time-lapse images were acquired with a Marianas imaging system (3I) equipped with an inverted spinning-disk confocal microscope (Axio-Observer Z1; Zeiss) and a Yokogawa CSU-X1 M1 confocal scanner. Cells were placed in heated sample chamber (37°C) and controlled CO$_2$. A 63× 1.2 W C-Apochromat Corr working distance = 0.28 M27 objective was used, and all the images were acquired by an sCMOS (Andor) Neo camera and Slidebook 5.0 software (3I). Analyses of the video frames were performed with Image Pro Plus 7.0.

## EM

For transmission EM, cells grown on glass coverslips were fixed, osmicated, dehydrated in a graded ethanol series and acetone, and infiltrated gradually with epon (TAAB) as described by Puhka et al. (2007). 60-nm-thick sections were cut parallel to the coverslip and poststained with uranyl acetate and lead citrate. Specimens were observed using a Tecnai 12 (FEI) microscope equipped with an Orius SC 1000B bottom-mounted charge-coupled device camera (Gatan) at acceleration voltage of 80 kV.

The negative-staining samples were prepared by mixing 2 µM protein with 500 µM unilamellar vesicles (with a diameter of 400 nm) in 20 mM Hepes buffer, pH 7.5, and 150 mM NaCl at RT for 5 min. The mixture was applied to the glow-discharged Pioloform (Agar Scientific)- and carbon-coated copper grids and stained with 3% uranyl acetate. At each step, excess solution was removed by filter paper. The membrane morphologies were examined with a JEM-1400 (Jeol) with a Orius SC 1000B bottom-mounted charge-coupled device camera (Gatan). The lipid composition of MIM used for EM was POPC:POPE:POPS:PI(4,5)P$_2$:cardiolipin = 40:34:3:5:18. The final concentrations of FAM92A1 and lipid were 2 and 500 µM, respectively.

## ImmunoEM

For preembedding immunoEM, U2OS cells were grown on coverslips and fixed with PLP fixative (2% formaldehyde, 0.01 M periodatem, and 0.075 M lysine-HCl in 0.075 M phosphate buffer, pH 7.4) for 2 h at RT as described previously (Uchiyama et al., 2002). Cells were permeabilized with 0.05% saponin (Sigma-Aldrich) and immunolabeled using anti-FAM92A1 antibody in 1:50 dilution followed by immunostaining with Nanogold α-rabbit IgG (Nanoprobes) in 1:60 dilution. Nanogold was silver enhanced using the HQ Silver kit (Nanoprobes) for 5 min and gold toned with 0.05% gold chloride. After washing, the cells were further processed for embedding.

## APEX2 staining for EM

Staining for APEX was performed essentially as described by Martell et al. (2012). Briefly, the cell monolayers expressing FAM92A1-APEX were fixed with 2% glutaraldehyde (EM grade; Sigma-Aldrich) in 0.1 M sodium cacodylate (NaCac) buffer, pH 7.4, supplemented with 2 mM CaCl$_2$ for 20 min at RT. After fixation, the cells were rinsed with chilled buffer and quenched in NaCac buffer containing 20 mM glycine for 5 min. After washing, the cells were incubated in 0.1 M NaCac buffer containing 0.1%

DAB (3,3′-diaminobenzidine tetra-HCl; TAAB), 0.02% H$_2$O$_2$, and 2 mM CaCl$_2$ on ice. After 30-min incubation in dark, the reaction medium was removed, and cells were washed three times with chilled NaCac buffer and postfixed with 1% reduced osmium tetroxide (Electron Microscopy Sciences) in chilled buffer for 1 h. Specimens were then dehydrated in a graded ethanol series and acetone, infiltrated with epon resin (TAAB), embedded, sectioned, and analyzed by transmission EM as described above.

## Electron tomography (ET)

The specimens for ET were chemically fixed and flat embedded as described for transmission EM. 250-nm-semithick sections were imaged using a Tecnai FEG 20 (FEI) operating at 200 kV. Images were collected with a 4,000 × 4,000–pixel Ultrascan 4000 charge-coupled device camera (Gatan) at nominal magnification of 9,600×, providing a 2× binned pixel size of 2.3 nm. The specimens were tilted at 1° intervals using a high-tilt specimen holder (model 2020; E.A. Fischione Instruments Inc.) between ±60°. Automated acquisition of dual-axis tilt series were performed using SerialEM software (Mastronarde, 2005). The alignment of tilt series and reconstructions were done with the IMOD software package (Kremer et al., 1996) using 10-nm colloidal gold particles underneath and on top of the sections as fiducial markers. Tomographic reconstructions were segmented and modeled using the Microscopy Image Browser (Belevich et al., 2016) and Amira (FEI).

## Western blotting

U2OS cells and homogenized mouse tissues were lysed for 10 min at 4°C with radioimmunoprecipitation assay (RIPA) lysis buffer (50 mM Tris, 150 mM NaCl, 0.1% SDS, 0.5% sodium deoxycholate, 1% Triton X-100, 1 mM PMSF, 10 mM sodium azide, 10 mM sodium ascorbate, and 5 mM Trolox). The lysates were briefly sonicated before centrifugation at 13,000 rpm for 10 min at 4°C. The protein concentrations were determined by Bradford assays (Pierce). Proteins were separated on SDS-PAGE gels and probed using the indicated antibodies. The following antibodies and dilutions were used: anti-FAM92A1 (1:500; HPA034760; Sigma-Aldrich), anti-TOM20 (1:500; sc-17764; Santa Cruz Biotechnology), anti-GAPDH (1:10,000; G8795; Sigma-Aldrich), antitubulin (1:10,000; T5168; Sigma-Aldrich), anti-COXIV (1:500; MA5-15087; Thermo Fisher Scientific); anti-Hsp60 (1:500; SMC-110; Biosite), anti-TOM40 (1:500; sc-365466; Santa Cruz Biotechnology), anti-TIM44 (1:500; sc-390755; Santa Cruz Biotechnology), anti-MRPL45 (1:3,000 15682-1-AP; ProteinTech), anti-ATP5A (1:500; ab14748; Abcam), anti-VDAC (1:500; AB10527; EMD Millipore), anticalnexin (1:200; ab112995; Abcam), PDI (1:200; ADI-SPA-891-F; Enzo), anti-MINOS1 (1:500; ARP44801-P050; Aviva System Biology), anti-CYTB (1:1,000; 55090-1-AP; ProteinTech), anti-SDHA (1:10,000; ab14715; Abcam), anti-NDUFA9 (1:1,000; 20312-1-AP; ProteinTech), and anti-GFP (1:4,000; 50430-2-AP; ProteinTech). Anti–cytochrome c (1:10,000; 05-479; EMD Millipore) was a gift from D. Lindholm (Faculty of Medicine, University of Helsinki, Helsinki, Finland). HRP-linked secondary antibodies (1:10,000; Promega) and ECL reagent (GE Healthcare) were applied for chemiluminescence detection of the blots.

Wang et al.
Regulation of mitochondrial ultrastructure by FAM92A1

Journal of Cell Biology    106
https://doi.org/10.1083/jcb.201806191

## Isolation and purification of mitochondria

Mitochondria were isolated and purified as described previously (Frezza et al., 2007). Briefly, cells were washed in precold PBS and resuspended in homogenization buffer (10 mM Tris-MOPS, 1 mM EGTA, and 200 mM sucrose, pH 7.4). Cell suspension was homogenized with a rotating Teflon potter (Potter S; Braun). Nonlysed cells were sedimented at 600 $g$ and discarded. The supernatant was subsequently centrifuged at 7,000 $g$, and the resulting pellet was the mitochondrial fraction.

Rat liver mitochondria were isolated essentially as described previously (Cascone et al., 2012). In brief, male Wistar rats (150–180 g) were killed by decapitation under $CO_2$ anesthesia. The liver was excised, cut in pieces, and homogenized using a Teflon potter (0.2 mm) in isolation medium containing 250 mM sucrose, 10 mM Hepes-KOH, and 1 mM EGTA, pH 7.4. The liver homogenate was filtered through cheesecloth and centrifuged at 800 $g$ for 8 min. The resulting supernatant was collected and centrifuged at 10,000 $g$ for 10 min. The resulting pellet was resuspended in 40 ml isolation medium, whereupon it was centrifuged at 10,000 $g$ for 10 min. The pellet was collected and resuspended at a protein concentration of ~80 mg/ml in isolation medium. All mitochondrial isolation steps were performed at 4°C.

## Proteolysis of mitochondria

Mitochondria were subfractionated to obtain mitoplasts by using a phosphate swelling–shrinking method (Bijur and Jope, 2003; Kang et al., 2007). Briefly, for breaking the MOM, purified mitochondrial pellets were suspended in swelling buffer (10 mM $KH_2PO_4$, pH 7.4) and incubated for 20 min with gentle mixing. To keep the mitoplasts intact, mitochondria were mixed with equal volume of shrinking buffer (10 mM $KH_2PO_4$, pH 7.4, 32% sucrose, 30% glycerol, and 10 mM $MgCl_2$) for another 20 min. The purified mitochondria and mitoplasts were suspended in homogenization buffer (10 mM Tris-MOPS, 1 mM EGTA, and 200 mM sucrose, pH 7.4) and treated with 0.2 mg/ml proteinase K with or without the presence of 1% NP-40 for 30 min. NP-40 was used to gently permeabilize mitochondrial membranes to allow proteinase K to enter mitochondria. Proteinase K activity was quenched with 2 mM PMSF for 10 min. All steps were performed on ice. 1% SDS was added to solubilize mitochondrial proteins, and the samples were blotted as indicated.

## Alkaline extraction of mitochondrial proteins

The purified mitochondria were resuspended in 0.1 M $Na_2CO_3$, pH 11, 11.5, or 12, or PBS, pH 7.4, on ice for 30 min with occasional vortex mixing and then centrifuged at 51,000 rpm for 30 min at 4°C using an Optima ultracentrifuge with a TLA 120 rotor (Beckman Coulter). The membrane pellets were dissolved in Laemmli loading buffer (2% SDS, 10% glycerol, 60 mM Tris-HCl, and 0.005% bromophenol blue). Supernatants were precipitated using TCA with a final concentration of 13% on ice for 30 min. After centrifugation at 20,000 $g$ for 30 min, pellets were washed two times with ice-cold acetone and dissolved in Laemmli loading buffer. The initial total mitochondria used for alkaline extraction, pellets, and supernatant were subjected to SDS-PAGE and Western blotting analysis.

## Measurement of mitochondrial membrane potential ($\Delta\Psi$m)

Mitochondrial membrane potential was measured using the fluorescent dye tetramethylrhodamine, methyl ester (TMRM; T668; Thermo Fisher Scientific). After treatment with FAM92A1 siRNA for 20 h, WT FAM92A was transiently expressed for 48 h. Cells treated with siRNA for 68 h were harvested, washed, and resuspended in DMEM without the phenol indicator. Cells were then stained with 50 nM TMRM for 15 min at 37°C. TMRM fluorescence was measured by a Varioskan LUX multimode microplate reader (Thermo Fisher Scientific) with SkanIt Software 5.0, excited at 549 nm, and recorded at 580 nm. The total mitochondrial mass was assessed by staining cells with MitoTracker green FM (M7514; Thermo Fisher Scientific), a mitochondrial marker regardless of mitochondrial membrane potential. The TMRM fluorescence intensity was normalized to mitochondrial mass.

## Detection of cellular and mitochondrial reactive oxygen species (ROS)

Cellular superoxide anions were detected and quantified using dihydroethidium (D1168; Thermo Fisher Scientific). After treatment with FAM92A1 siRNA for 20 h, WT FMA92A1 or mutants were transiently expressed for another 24 or 48 h. U2OS cells were harvested, washed, and incubated with 10 μM DHE dissolved in prewarmed PBS for 15 min in the dark. The fluorescence intensity was recorded using a Varioskan LUX multimode microplate reader (Thermo Fisher Scientific) with excitation and emission at 510 and 600 nm, respectively. The total mitochondrial mass was evaluated by staining the cells with MitoTracker green FM (M7514; Molecular Probes). The changes in fluorescence intensity of DHE were normalized to mitochondrial mass.

Mitochondrial superoxide production in FAM92A1-knockdown cells was detected using a mitochondrial superoxide indicator MitoSOX for live-cell imaging (M36008; Molecular Probes). After treatment with FAM92A1 siRNA for 20 h, WT FMA92A1 or mutants were transiently expressed for another 24 or 48 h. Cells were harvested and washed with warm HBSS followed by dark incubation in HBSS containing 1 μM MitoSOX at 37°C for 10 min. After removal of excess MitoSOX, the cells were replated in 96-well microplates. The MitoSOX fluorescence was measured using Varioskan LUX multimode microplate reader (SkanIt Software 4.1) with excitation and emission at 510 nm and 580 nm, respectively. The total mitochondrial mass was evaluated by staining the cells with MitoTracker green FM (M7514; Molecular Probes). The changes in fluorescence intensity of MitoSOX were normalized to mitochondrial mass.

## Assessment of ATP production

Cellular ATP levels were detected by an ATP determination kit (A22066; Thermo Fisher Scientific) according to the manufacturer's instructions. After treatment with FAM92A1 siRNA for 20 h, WT FMA92A1 or mutants were transiently expressed for another 24 or 48 h. Cells were harvested, washed with PBS one time, and centrifuged at 600 $g$ for 10 min at 4°C. Cells were lysed on ice for 10 min by RIPA lysis buffer, and the cell lysates were briefly sonicated and centrifuged at 13,000 rpm for 10 min at 4°C. 10 μl cell supernatant was mixed with 90 μl reaction solution,

Wang et al.
Regulation of mitochondrial ultrastructure by FAM92A1

Journal of Cell Biology    107
https://doi.org/10.1083/jcb.201806191

and the luminescence was measured by a multimode plate reader (Varioskan Flash; Thermo Fisher Scientific). The amounts of ATP were calculated from the standard curve and normalized to the total amount of protein used for detection of cellular ATP levels. The statistics were done with Student's $t$ test. Data are presented as mean ± SEM of three replicates.

### Assessment of enzyme activity

After treatment with FAM92A1 siRNA for 20 h, WT FMA92A1 were transiently expressed for 48 h. Cells were harvested, and mitochondria were isolated for mitochondrial respiratory chain enzymatic activity assays. The activities of complex I and citrate synthase were measured by spectrophotometry using Ultrospec 3000 pro UV/visible spectrophotometer (Pharmacia Biotech) as previously described (Spinazzi et al., 2012). For complex I activity, 75 µg mitochondrial proteins were dissolved in 50 mM potassium phosphate buffer, pH 7.5, containing 3 mg/ml BSA, 0.3 mM KCN, and 0.1 mM NADH with and without 10 µM rotenone. After preincubating for 2 min, the reaction was started by adding ubiquinone to a final concentration of 60 µM. Decrease of absorbance at 340 nm was recorded for 2 min. The complex I activity was normalized to the protein amount and then was further normalized to the corresponding activity of citrate synthase. For citrate synthase activity, 18 µg mitochondrial protein was dissolved in 100 mM Tris buffer, pH 8.0, with 0.2% Triton X-100 containing 0.1 mM DTNB and 0.3 mM acetyl-CoA. After incubation for 2 min, the reaction was started by adding oxaloacetic acid to a final concentration of 0.5 mM. Increase in absorbance at 412 nm was recorded for 3 min. The citrate synthase activity was normalized to the total protein amount.

The activity of complex IV was determined using the cytochrome c oxidase assay kit (Sigma-Aldrich) according to the manufacturer's instructions. Decrease in absorbance at 550 nm of ferrocytochrome c was recorded using Ultrospec 3000 pro UV/visible spectrophotometer (Bio-Rad). The cytochrome c oxidase assay was performed as described by Spinazzi et al. (2012). The complex IV activity was normalized to the total protein amount and further normalized to the corresponding activity of citrate synthase.

### Measurement of cellular metabolism

The cellular OCR were measured using a Seahorse XF96$^e$ analyzer (Seahorse Bioscience; Agilent Technologies). The XF96 sensor cartridge was activated with 200 µl XF96 calibrant solution per well for 12 h at 37°C. U2OS cells were seeded onto XF96 cell culture microplates at $10^4$ cells per well. After treatment with FAM92A1 siRNA for 20 h, WT FMA92A1 or mutants were transiently expressed for another 24 or 48 h. 1 h before measurement, the culture medium was changed to serum-free and bicarbonate-free DMEM supplemented with 10 mM glucose, 5 mM pyruvate, and 5 mM glutamine. After incubation for 1 h at 37°C in a non-CO$_2$ incubator, steady-state and postintervention analyses were performed. Respiration was assessed by injection of oligomycin (1 µM) to inhibit the mitochondrial ATP synthase, carbonyl cyanide-p-trifluoromethoxy-phenylhydrazone (FCCP; 1 µM) to collapse the mitochondrial membrane potential, and rotenone (1 µM) and antimycin A (1 µM) to inhibit the respiratory chain.

The OCR was measured before and after the addition of inhibitors at indicated times. The OCR was normalized to total protein amount (micrograms).

### Blue-native PAGE

The blue-native gel electrophoresis was performed using the NativePAGE Novex Bis-Tris gel system (BN1001BOX; Invitrogen) according to the manufacturer's protocol. Briefly, mitochondria were suspended in 1% DDM in PBS on ice for 30 min and centrifuged at 22,000 $g$ for 30 min. The supernatant was supplemented with 0.2% Coomassie blue G250 dye and loaded on a 3–12% gradient NativePAGE gel. Proteins were transferred to the polyvinylidene fluoride membrane (EMD Millipore), which was subsequently incubated in 8% acetic acid and activated with methanol. The proteins were blotted using the indicated antibodies.

### RNA and DNA isolation for real-time quantitative PCR (RT-qPCR)

Total RNA was extracted from the whole cells using the GeneJET RNA purification kit (K0731; Thermo Fisher Scientific). Single-stranded cDNA was synthesized from extracted mRNA with a Maxima first-strand cDNA synthesis kit (K1671; Thermo Fisher Scientific). For quantification of mitochondrial (mtDNA) copy numbers, total DNA was extracted from the cells after treatment with control or FAM92A1 siRNA for 72 h using a total DNA, RNA, and protein isolation kit (Macherey-Nagel) following the manufacturer's instructions. The mtDNA level was assessed using RT-qPCR analyses. qPCR reactions were performed with Maxima SYBR Green/ROX (K0221; Thermo Fisher Scientific) by CFX96 (Bio-Rad). The transcription level of FAM92A1 and mtDNA copy number were calculated with the $2^{-\Delta\Delta Ct}$ method. Primers used in this study were *FAM92A1* forward, 5′-TCGACAAGCAGAGGTTGAAA-3′, and reverse, 5′-TCGATTCCTTGCTGTGAGTG-3′; mtDNA forward, 5′-ACCACAGTTTCATGCCCATCGT-3′, and reverse, 5′-TTTATGGGCTTTGGTGAGGGAGGT-3′; and *β-globin* forward, 5′-GGTGAAGGCTCATGGCAAGAAAG-3′, and reverse, 5′-GTCACAGTGCAGCTCACTCAGT-3′.

### Production of recombinant proteins and dimerization of FAM92A1

FAM92A1 and the BAR domain were expressed as his-tagged fusion proteins using BL21 (DE3) cells at 16°C for 18 h with 0.8 mM IPTG induction. Pellets were resuspended in lysis buffer (20 mM Tri-HCl pH 8.8, 300 mM NaCl, and 1 mM CHAPS) supplemented with protease inhibitor PMSF. Cells were lysed by Emulsiflex C-3 and subsequently centrifuged for 30 min at 15,000 $g$. Supernatants were incubated with Ni-NTA Superflow beads (QIAGEN) for 2 h at 4°C, eluted with imidazone gradient, and further purified with anion ion exchange chromatography column (HiTrap Q HP; GE Healthcare) using FPLC (GE Healthcare). The oligomeric state of FAM92A1 BAR domain was measured using multiangle laser light scattering (LS/RI detector; Wyatt) combined with high-performance liquid chromatography (Shimadzu). The protein was loaded onto a Superdex 200 10/300 column at 4°C, and flow rate was 0.5 ml/min. The data were analyzed using Astra 6.1 provided by Wyatt.

Wang et al.
Regulation of mitochondrial ultrastructure by FAM92A1

**Journal of Cell Biology**    108
https://doi.org/10.1083/jcb.201806191

## Vesicle preparation and membrane-binding assays

Lipids in desired concentrations were mixed and dried under a stream of nitrogen. The lipids were subsequently maintained under reduced pressure for at least 4 h. The dry lipids were then hydrated in 20 mM Hepes, pH 7.5, and 150 mM NaCl to obtain multilamellar vesicles. To obtain unilamellar vesicles for EM experiments, vesicles were extruded though a polycarbonate filter (400-nm pore size) using a mini extruder (Avanti Polar Lipids). For vesicle cosedimentation assays, proteins and liposomes were incubated at RT for 15 min and centrifuged at 100,000 rpm with a TLA 100 rotor (Beckman Coulter) for 30 min to separate membrane-bound (pellets) and membrane-free fractions (supernatants). The final concentrations of FAM92A1 and liposomes were 2 µM and 500 µM, respectively, in 20 mM Hepes buffer, pH 7.5, with 150 mM NaCl. Equal proportions of supernatants and pellets were loaded for SDS-PAGE. After electrophoresis, the gels were stained with Coomassie blue. The intensities of the FAM92A1 bands were quantified by Quantity One program (Bio-Rad). Vesicle coflotation assays were performed according to (Pykäläinen et al., 2011) with a slight modification. For visualization, liposomes were labeled with 2% Rhodamine B–conjugated PE (Avanti Polar Lipids; Sigma-Aldrich). 2.5 µM protein was mixed with liposomes with a lipid concentration of 333 µM, and the mixture was incubated at RT for 15 min. After loading the sucrose gradient, the samples were centrifuged at 4°C for 30 min at 54,000 rpm with Optima Max using a TLS55 rotor (Beckman Coulter). 100-µl fractions were collected from top to bottom, and the samples were run on SDS-PAGE.

In vesicle cosedimentation/coflotation assays, the lipid compositions used for MOM and MIM were POPC:POPE:POPS:PI(4,5)P$_2$:liverPI:POPA:cardiolipin:RhodaminePE = 54:27:2:5:8:1:1:2 and POPC:POPE:POPS:PI(4,5)P$_2$:cardiolipin:RhodaminePE = 40:32:3:5:18:2, respectively (Watt et al., 2002; Horvath and Daum, 2013). In vesicle cosedimentation assays for lipid-binding specificity of FAM92A1, PI(4,5)P$_2$ was included as the same amount as cardiolipin in vivo (18% in the MIM). The lipid compositions were PC:PE:RhodaminePE = 66:32:2, POPC:POPE:PI(4,5)P$_2$:RhodaminePE = 48:32:18:2, and POPC:POPE:cardiolipin:RhodaminePE = 48:32:18:2. The final protein and lipid concentrations used were 2 and 500 µM, respectively.

Fluorescence anisotropy of DPH was measured with a PerkinElmer LS 55 spectrometer with excitation at 360 nm and emission at 450 nm and using 10-nm bandwidths. The lipid compositions used for the MOM, MIM, and MIM without cardiolipin were POPC:POPE:POPS:PI(4,5)P$_2$:liverPI:POPA:cardiolipin:DPH = 54:29:2:5:8:1:1:0.002, POPC:POPE:POPS:PI(4,5)P$_2$:cardiolipin:DPH = 40:34:3:5:18:0.002, and POPC:POPE:POPS:PI(4,5)P$_2$:DPH = 58:34:3:5:0.002, respectively. The final lipid concentration was 40 µM.

## Giant vesicle preparation and membrane morphology assay

Giant vesicles were prepared as described previously (Weinberger et al., 2013). Briefly, 5% (wt/wt) Poly(vinyl alcohol) solution was spread on a coverslip and dried at 40°C for 30 min. The coverslip was subsequently maintained under vacuum at RT for 30 min. 1 ml swelling buffer (20 mM Tris-HCl, pH 7.5, 50 mM NaCl, and 20 mM sucrose) was supplied on the coverslip, and giant vesicles were harvested after 1 h. The lipid composition was POPC:POPE:POPS:PI(4,5)P$_2$:cardiolipin = 40:34:3:5:18, and 0.5% Bodipy TR ceramide was added as a fluorescent probe. 0.2 µM FAM92A1 was mixed with the giant vesicles and incubated at RT for 20 min. The membrane morphology was imaged with a Leica TCS SP8 X confocal microscope using a 63× 1.2 W (HC Plan Apochromat CS2) objective.

## Quantification and statistical analysis
### Quantitative immunoEM

To determine the submitochondrial localization of FAM92A1, the postembedding immunogold labeling of FAM92A1 in U2OS was counted using ImageJ (National Institutes of Health) as described previously with slight modifications (Vogel et al., 2006). Mitochondria were partitioned into the representing regions of the MOM/IBM and CM for quantification of immunogold particle distribution. The number of gold particles on CM or MOM/IBM was normalized to the corresponding membrane length (nanometers). 16 mitochondria and 595 particles were used for analysis.

### Quantification of tubule diameter, mitochondria, and cristae morphology

For the analysis of mitochondrial cristae morphology, 200 mitochondria were counted from control or FAM92A1 siRNA–treated cells and scored for normal (lamellar) or ballooned and swollen cristae (disorganized). The mitochondrial diameter, length of cristae, crista junction opening, and number of lamellar cristae were measured using ImageJ. At least 100 mitochondria were applied for measuring the tubule diameter and cristae morphology analysis, respectively. The total number of lamellar cristae from each mitochondrial were normalized to the mitochondrial length (micrometers).

### Quantification of membrane binding

The intensity of the bands was quantified using Image Lab 6.0 (volume tool). For cosedimentation assays, the membrane-binding percentage was calculated by the intensity of protein in the pellet divided by the intensity of total protein (supernatant plus pellet). The protein control was deducted to get the actual binding percentage. For coflotation assays, the membrane binding was calculated using the protein intensity in the liposome fraction divided by the intensity sum of all the fractions. The protein control was deducted to get the actual membrane binding.

## Statistical analysis

Differences among groups were performed using the unpaired Student's $t$ test. All data were reported as mean ± SEM or SD as indicated in the figure legends.

## Online supplemental material

Fig. S1 shows FAM92A1 as a BAR domain protein. Fig. S2 shows the ubiquitous expression, membrane binding, and remodeling activity of FAM92A1. Fig. S3 shows the rescue of mitochondrial morphology by WT FAM92A1 and mutants with defects in membrane binding and remodeling. Video 1 shows the mitochondrial dynamics in U2OS cells expressing mito-YFP after 72 h control siRNA treatment. Video 2 shows the mitochondrial dynamics in

U2OS cells expressing mito-YFP after 72 h FAM92A1 siRNA treatment. Video 3 shows the normal cristae architecture in control U2OS cells. Video 4 shows the severe changes in mitochondrial ultrastructure by FAM92A1 silencing. Video 5 shows the severe changes of mitochondrial ultrastructure after FAM92A1 silencing. Video 6 shows the normal crista junction in control U2OS cells. Video 7 shows the changes of mitochondrial crista junctions after FAM92A1 silencing.

## Acknowledgments

## References

Barbot, M., D.C. Jans, C. Schulz, N. Denkert, B. Kroppen, M. Hoppert, S. Jakobs, and M. Meinecke. 2015. Mic10 oligomerizes to bend mitochondrial inner membranes at cristae junctions. *Cell Metab.* 21:756–763. https://doi.org/10.1016/j.cmet.2015.04.006

Belevich, I., M. Joensuu, D. Kumar, H. Vihinen, and E. Jokitalo. 2016. Microscopy Image Browser: A Platform for Segmentation and Analysis of Multidimensional Datasets. *PLoS Biol.* 14:e1002340. https://doi.org/10.1371/journal.pbio.1002340

Bijur, G.N., and R.S. Jope. 2003. Rapid accumulation of Akt in mitochondria following phosphatidylinositol 3-kinase activation. *J. Neurochem.* 87:1427–1435. https://doi.org/10.1046/j.1471-4159.2003.02113.x

Bohnert, M., R.M. Zerbes, K.M. Davies, A.W. Mühleip, H. Rampelt, S.E. Horvath, T. Boenke, A. Kram, I. Perschil, M. Veenhuis, et al. 2015. Central role of Mic10 in the mitochondrial contact site and cristae organizing system. *Cell Metab.* 21:747–755. https://doi.org/10.1016/j.cmet.2015.04.007

Boucrot, E., A. Pick, G. Çamdere, N. Liska, E. Evergren, H.T. McMahon, and M.M. Kozlov. 2012. Membrane fission is promoted by insertion of amphipathic helices and is restricted by crescent BAR domains. *Cell.* 149:124–136. https://doi.org/10.1016/j.cell.2012.01.047

Campelo, F., H.T. McMahon, and M.M. Kozlov. 2008. The hydrophobic insertion mechanism of membrane curvature generation by proteins. *Biophys. J.* 95:2325–2339. https://doi.org/10.1529/biophysj.108.133173

Cascone, A., C. Bruelle, D. Lindholm, P. Bernardi, and O. Eriksson. 2012. Destabilization of the outer and inner mitochondrial membranes by core and linker histones. *PLoS One.* 7:e35357. https://doi.org/10.1371/journal.pone.0035357

Cogliati, S., J.A. Enriquez, and L. Scorrano. 2016. Mitochondrial Cristae: Where Beauty Meets Functionality. *Trends Biochem. Sci.* 41:261–273. https://doi.org/10.1016/j.tibs.2016.01.001

Daumke, O., A. Roux, and V. Haucke. 2014. BAR domain scaffolds in dynamin-mediated membrane fission. *Cell.* 156:882–892. https://doi.org/10.1016/j.cell.2014.02.017

Davies, K.M., C. Anselmi, I. Wittig, J.D. Faraldo-Gómez, and W. Kühlbrandt. 2012. Structure of the yeast F1Fo-ATP synthase dimer and its role in shaping the mitochondrial cristae. *Proc. Natl. Acad. Sci. USA.* 109:13602–13607. https://doi.org/10.1073/pnas.1204593109

Frezza, C., S. Cipolat, and L. Scorrano. 2007. Organelle isolation: functional mitochondria from mouse liver, muscle and cultured fibroblasts. *Nat. Protoc.* 2:287–295. https://doi.org/10.1038/nprot.2006.478

Friedman, J.R., and J. Nunnari. 2014. Mitochondrial form and function. *Nature.* 505:335–343. https://doi.org/10.1038/nature12985

Frost, A., V.M. Unger, and P. De Camilli. 2009. The BAR domain superfamily: membrane-molding macromolecules. *Cell.* 137:191–196. https://doi.org/10.1016/j.cell.2009.04.010

Gallop, J.L., C.C. Jao, H.M. Kent, P.J.G. Butler, P.R. Evans, R. Langen, and H.T. McMahon. 2006. Mechanism of endophilin N-BAR domain-mediated membrane curvature. *EMBO J.* 25:2898–2910. https://doi.org/10.1038/sj.emboj.7601174

Guarani, V., E.M. McNeill, J.A. Paulo, E.L. Huttlin, F. Fröhlich, S.P. Gygi, D. Van Vactor, and J.W. Harper. 2015. QIL1 is a novel mitochondrial protein required for MICOS complex stability and cristae morphology. *eLife.* 4:1–23. https://doi.org/10.7554/eLife.06265

Habermann, B. 2004. The BAR-domain family of proteins: a case of bending and binding? *EMBO Rep.* 5:250–255. https://doi.org/10.1038/sj.embor.7400105

Herrmann, J.M. 2011. MINOS is plus: a Mitofilin complex for mitochondrial membrane contacts. *Dev. Cell.* 21:599–600. https://doi.org/10.1016/j.devcel.2011.09.013

Hessenberger, M., R.M. Zerbes, H. Rampelt, S. Kunz, A.H. Xavier, B. Purfürst, H. Lilie, N. Pfanner, M. van der Laan, and O. Daumke. 2017. Regulated membrane remodeling by Mic60 controls formation of mitochondrial crista junctions. *Nat. Commun.* 8:15258. https://doi.org/10.1038/ncomms15258

Horvath, S.E., and G. Daum. 2013. Lipids of mitochondria. *Prog. Lipid Res.* 52:590–614. https://doi.org/10.1016/j.plipres.2013.07.002

Kang, B.H., J. Plescia, T. Dohi, J. Rosa, S.J. Doxsey, and D.C. Altieri. 2007. Regulation of tumor cell mitochondrial homeostasis by an organelle-specific Hsp90 chaperone network. *Cell.* 131:257–270. https://doi.org/10.1016/j.cell.2007.08.028

Kremer, J.R., D.N. Mastronarde, and J.R. McIntosh. 1996. Computer visualization of three-dimensional image data using IMOD. *J. Struct. Biol.* 116:71–76. https://doi.org/10.1006/jsbi.1996.0013

Kühlbrandt, W. 2015. Structure and function of mitochondrial membrane protein complexes. *BMC Biol.* 13:89. https://doi.org/10.1186/s12915-015-0201-x

Mannella, C.A. 2006. Structure and dynamics of the mitochondrial inner membrane cristae. *Biochim. Biophys. Acta.* 1763:542–548. https://doi.org/10.1016/j.bbamcr.2006.04.006

Martell, J.D., T.J. Deerinck, Y. Sancak, T.L. Poulos, V.K. Mootha, G.E. Sosinsky, M.H. Ellisman, and A.Y. Ting. 2012. Engineered ascorbate peroxidase as a genetically encoded reporter for electron microscopy. *Nat. Biotechnol.* 30:1143–1148. https://doi.org/10.1038/nbt.2375

Mastronarde, D.N. 2005. Automated electron microscope tomography using robust prediction of specimen movements. *J. Struct. Biol.* 152:36–51. https://doi.org/10.1016/j.jsb.2005.07.007

McMahon, H.T., and E. Boucrot. 2015. Membrane curvature at a glance. *J. Cell Sci.* 128:1065–1070. https://doi.org/10.1242/jcs.114454

McMahon, H.T., and J.L. Gallop. 2005. Membrane curvature and mechanisms of dynamic cell membrane remodelling. *Nature.* 438:590–596. https://doi.org/10.1038/nature04396

Milenkovic, D., and N.-G. Larsson. 2015. Mic10 Oligomerization Pinches off Mitochondrial Cristae. *Cell Metab.* 21:660–661. https://doi.org/10.1016/j.cmet.2015.04.020

Mim, C., and V.M. Unger. 2012. Membrane curvature and its generation by BAR proteins. *Trends Biochem. Sci.* 37:526–533. https://doi.org/10.1016/j.tibs.2012.09.001

Mim, C., H. Cui, J.A. Gawronski-Salerno, A. Frost, E. Lyman, G.A. Voth, and V.M. Unger. 2012. Structural basis of membrane bending by the N-BAR protein endophilin. *Cell.* 149:137–145. https://doi.org/10.1016/j.cell.2012.01.048

Paumard, P., J. Vaillier, B. Coulary, J. Schaeffer, V. Soubannier, D.M. Mueller, D. Brèthes, J.P. di Rago, and J. Velours. 2002. The ATP synthase is involved in generating mitochondrial cristae morphology. *EMBO J.* 21:221–230. https://doi.org/10.1093/emboj/21.3.221

Peter, B.J., H.M. Kent, I.G. Mills, Y. Vallis, P.J.G. Butler, P.R. Evans, and H.T. McMahon. 2004. BAR domains as sensors of membrane curvature: the amphiphysin BAR structure. *Science.* 303:495–499. https://doi.org/10.1126/science.1092586

Pfanner, N., M. van der Laan, P. Amati, R.A. Capaldi, A.A. Caudy, A. Chacinska, M. Darshi, M. Deckers, S. Hoppins, T. Icho, et al. 2014. Uniform nomenclature for the mitochondrial contact site and cristae organizing system. *J. Cell Biol.* 204:1083–1086. https://doi.org/10.1083/jcb.201401006

Pirozzi, F., F.R. Di Raimo, G. Zanni, E. Bertini, P. Billuart, T. Tartaglione, E. Tabolacci, A. Brancaccio, G. Neri, and P. Chiurazzi. 2011. Insertion of 16 amino acids in the BAR domain of the oligophrenin 1 protein causes mental retardation and cerebellar hypoplasia in an Italian family. *Hum. Mutat.* 32:E2294–E2307. https://doi.org/10.1002/humu.21567

Prinz, W.A., and J.E. Hinshaw. 2009. Membrane-bending proteins. *Crit. Rev. Biochem. Mol. Biol.* 44:278–291. https://doi.org/10.1080/10409230903183472

Puhka, M., H. Vihinen, M. Joensuu, and E. Jokitalo. 2007. Endoplasmic reticulum remains continuous and undergoes sheet-to-tubule transformation during cell division in mammalian cells. *J. Cell Biol.* 179:895–909. https://doi.org/10.1083/jcb.200705112

Pykäläinen, A., M. Boczkowska, H. Zhao, J. Saarikangas, G. Rebowski, M. Jansen, J. Hakanen, E.V. Koskela, J. Peränen, H. Vihinen, et al. 2011. Pinkbar is an epithelial-specific BAR domain protein that generates planar membrane structures. *Nat. Struct. Mol. Biol.* 18:902–907. https://doi.org/10.1038/nsmb.2079

Qualmann, B., D. Koch, and M.M. Kessels. 2011. Let's go bananas: revisiting the endocytic BAR code. *EMBO J.* 30:3501–3515. https://doi.org/10.1038/emboj.2011.266

Rabl, R., V. Soubannier, R. Scholz, F. Vogel, N. Mendl, A. Vasiljev-Neumeyer, C. Körner, R. Jagasia, T. Keil, W. Baumeister, et al. 2009. Formation of cristae and crista junctions in mitochondria depends on antagonism between Fcj1 and Su e/g. *J. Cell Biol.* 185:1047–1063. https://doi.org/10.1083/jcb.200811099

Saarikangas, J., H. Zhao, A. Pykäläinen, P. Laurinmäki, P.K. Mattila, P.K.J. Kinnunen, S.J. Butcher, and P. Lappalainen. 2009. Molecular mechanisms of membrane deformation by I-BAR domain proteins. *Curr. Biol.* 19:95–107. https://doi.org/10.1016/j.cub.2008.12.029

Safari, F., and S. Suetsugu. 2012. The BAR domain superfamily proteins from subcellular structures to human diseases. *Membranes (Basel).* 2:91–117. https://doi.org/10.3390/membranes2010091

Simunovic, M., G.A. Voth, A. Callan-Jones, and P. Bassereau. 2015. When Physics Takes Over: BAR Proteins and Membrane Curvature. *Trends Cell Biol.* 25:780–792. https://doi.org/10.1016/j.tcb.2015.09.005

Spinazzi, M., A. Casarin, V. Pertegato, L. Salviati, and C. Angelini. 2012. Assessment of mitochondrial respiratory chain enzymatic activities on tissues and cultured cells. *Nat. Protoc.* 7:1235–1246. https://doi.org/10.1038/nprot.2012.058

Strauss, M., G. Hofhaus, R.R. Schröder, and W. Kühlbrandt. 2008. Dimer ribbons of ATP synthase shape the inner mitochondrial membrane. *EMBO J.* 27:1154–1160. https://doi.org/10.1038/emboj.2008.35

Tarasenko, D., M. Barbot, D.C. Jans, B. Kroppen, B. Sadowski, G. Heim, W. Möbius, S. Jakobs, and M. Meinecke. 2017. The MICOS component Mic60 displays a conserved membrane-bending activity that is necessary for normal cristae morphology. *J. Cell Biol.* 216:889–899. https://doi.org/10.1083/jcb.201609046

Uchiyama, K., E. Jokitalo, F. Kano, M. Murata, X. Zhang, B. Canas, R. Newman, C. Rabouille, D. Pappin, P. Freemont, and H. Kondo. 2002. VCIP135, a novel essential factor for p97/p47-mediated membrane fusion, is required for Golgi and ER assembly in vivo. *J. Cell Biol.* 159:855–866. https://doi.org/10.1083/jcb.200208112

van der Laan, M., S.E. Horvath, and N. Pfanner. 2016. Mitochondrial contact site and cristae organizing system. *Curr. Opin. Cell Biol.* 41:33–42. https://doi.org/10.1016/j.ceb.2016.03.013

Vogel, F., C. Bornhövd, W. Neupert, and A.S. Reichert. 2006. Dynamic subcompartmentalization of the mitochondrial inner membrane. *J. Cell Biol.* 175:237–247. https://doi.org/10.1083/jcb.200605138

Wai, T., and T. Langer. 2016. Mitochondrial Dynamics and Metabolic Regulation. *Trends Endocrinol. Metab.* 27:105–117. https://doi.org/10.1016/j.tem.2015.12.001

Watt, S.A., G. Kular, I.N. Fleming, C.P. Downes, and J.M. Lucocq. 2002. Subcellular localization of phosphatidylinositol 4,5-bisphosphate using the pleckstrin homology domain of phospholipase C delta1. *Biochem. J.* 363:657–666. https://doi.org/10.1042/bj3630657

Weinberger, A., F.C. Tsai, G.H. Koenderink, T.F. Schmidt, R. Itri, W. Meier, T. Schmatko, A. Schröder, and C. Marques. 2013. Gel-assisted formation of giant unilamellar vesicles. *Biophys. J.* 105:154–164. https://doi.org/10.1016/j.bpj.2013.05.024

Zhao, H., A. Pykäläinen, and P. Lappalainen. 2011. I-BAR domain proteins: linking actin and plasma membrane dynamics. *Curr. Opin. Cell Biol.* 23:14–21. https://doi.org/10.1016/j.ceb.2010.10.005

Zhao, H., A. Michelot, E.V. Koskela, V. Tkach, D. Stamou, D.G. Drubin, and P. Lappalainen. 2013. Membrane-sculpting BAR domains generate stable lipid microdomains. *Cell Reports.* 4:1213–1223. https://doi.org/10.1016/j.celrep.2013.08.024